Indentation Size Effects in Single Crystal Copper as Revealed by Synchrotron X-ray Microdiffraction

G. Feng[a], A. S. Budiman, and W. D. Nix

Department of Materials Science & Engineering, Stanford University, Stanford, California 94305

N. Tamura

Advanced Light Source (ALS), Lawrence Berkeley National Laboratory (LBNL), Berkeley, California 94720

J. R. Patel

Department of Materials Science and Engineering, Stanford University, Stanford, California 94305 and Advanced Light Source (ALS), Lawrence Berkeley National Laboratory (LBNL), Berkeley, California 94720

ABSTRACT

The indentation size effect (ISE) has been observed in numerous nanoindentation studies on crystalline materials; it is found that the hardness increases dramatically with decreasing indentation size – a "smaller is stronger" phenomenon. Some have attributed the ISE to the existence of strain gradients and the geometrically necessary dislocations (GNDs). Since the GND density is directly related to the local lattice curvature, the Scanning X-ray Microdiffraction (μSXRD) technique, which can quantitatively measure relative lattice rotations through the streaking of Laue diffractions, can used to study the

[a] Present address: Division of Engineering, Brown University, Providence, RI 02912; electronic mail: gang_feng@brown.edu

strain gradients. The synchrotron μSXRD technique we use – which was developed at the Advanced Light Source (ALS), Berkeley Lab – allows for probing the local plastic behavior of crystals with sub-micrometer resolution. Using this technique, we studied the local plasticity for indentations of different depths in a Cu single crystal. Broadening of Laue diffractions (streaking) was observed, showing local crystal lattice rotation due to the indentation-induced plastic deformation. A quantitative analysis of the streaking allows us to estimate the average GND density in the indentation plastic zones. The size dependence of the hardness, as found by nanoindentation, will be described, and its correlation to the observed lattice rotations will be discussed.

I. INTRODUCTION

Modern devices are currently being aggressively scaled. Increasingly, the dimensions of these devices are at the sub-micrometer and nanometer scale. Although most of these devices are primarily functional and not mechanical, their reliability and lifetimes are often controlled by the mechanical properties of the materials that comprise the device. Thus, the creation of such small components requires a thorough understanding of the mechanical properties of materials at these small length scales. Furthermore, as specimens are reduced in size to the scale of the microstructure, their mechanical properties deviate from those of bulk materials. For example, in thin films – where only one dimension, the thickness, reaches the micron scale and below – the flow stress is found to be higher than its bulk value and becomes even higher as the film gets thinner. This size effect is usually attributed to the confinement of dislocations by the substrate.[1-3]

In nanoindentation experiments, where the length-scale of the deformation reaches the microstructural length-scale of the material, the governing relations between stress and strain deviate from the classical laws that apply to bulk materials. For crystalline materials, the hardness of a small indentation is usually higher than that of a large indentation. This indentation size effect (ISE) has been explained using the concept of geometrically necessary dislocations (GNDs) and strain gradients.[4-18] According to this picture, for a self-similar indenter, for example, a Berkovich-shape pyramidal indenter, the total length of GNDs forced into the solid by the indenter scales with the square of the indentation depth, while the volume in which these dislocations are found scales with the cube of the indentation depth; thus, the GND density (ρ_G) depends inversely on the

indentation depth. The higher dislocation densities expected at smaller indentation depths lead naturally to higher strengths through the Taylor relation,[19] and this leads to the ISE.

Characterizing the deformation zone below indentations has been a focus of many researchers.[20-23] In recent years, the use of focused ion beam (FIB) has enabled more accurate scanning electron microscope (SEM) imaging,[24-26] as well as crystal orientation mapping using electron backscatter diffraction (EBSD)[27,28] and transmission electron microscopy (TEM).[29,30] Scanning X-ray microdiffraction (μSXRD) using a focused polychromatic/white synchrotron X-ray beam can be used to determine the lattice rotation which is directly related to the local lattice curvature,[31] strain gradients, and the GND density. Compared to many other techniques, such as EBSD and TEM, two advantages of μSXRD are non-destructive and a much larger detection depth. μSXRD has been described in a complete manner in the literature,[32] and its capability as a local plasticity probe at small scales stems from the high brilliance of the synchrotron source, as well as the recent advances in X-ray focusing optics. This capability is also related to the continuous range of wavelengths in a white X-ray beam, allowing Bragg's law to be satisfied even when the lattice is locally rotated or bent, resulting in the observation of streaked Laue spots. μSXRD has been used in the study of the early stages of electromigration failure in metallic interconnect lines,[33,34] wherein lattice bending and GNDs are created by electromigration processes.[33,34]

The use of spatially resolved X-ray diffraction to measure local lattice rotations induced by indentation was pioneered by Ice's group.[35-40] In particular, they have provided a methodology for a clean measurement of lattice rotation associated with a 2μm-deep Berkovich indentation.[35,36] They demonstrated that,[35,36] at the center of one

particular indentation side-face (position *A* as shown in Fig. 2(a)), the X-ray beam encounters a single rotation axis; at other positions, the X-ray beam may encounter multiple rotation axes, which complicates the resulting diffracted beams.

The present study builds upon and is complementary to this body of knowledge, and our primary focus is to compare ρ_G estimated through the observed lattice rotation to that expected from nanoindentation hardness results. Using μSXRD, we quantitatively study the streaking/broadening of Cu Laue peaks corresponding to different indentation depths, allowing us to estimate ρ_G in the individual indentation-induced plastic zones. Then, a revised Nix and Gao model[16,17] is used to correlate the experimental hardness measurement with ρ_G. Finally, the values of ρ_G estimated through both μSXRD observation and hardness measurement will be compared and discussed.

II. EXPERIMENTAL

A copper single crystal specimen with a <111> out-of-plane orientation, in the form of a 2mm-thick, 10mm-diameter disk, was purchased from Monocrystals Company. A flat edge was cut along a <110> direction (normal to a <112> direction) to provide a reference for the crystal orientation. The indented sample surface was mirror-finished and electropolished.

Three-sided Berkovich indentation tests were performed using a Nanoindenter XP™ with the continuous stiffness measurement module. Figure 1 shows an optical image of the 5 indentation arrays (each consisting of 8 indents, namely a 3×3 array without the center), corresponding to indentation depths of 3μm, 1.5μm, 1μm, 0.5μm and 0.25μm.

The horizontal edges of the indents were lined up within 1° to the flat edge, namely a <110> type direction of the single Cu disk as shown in Figs. 1 and 2(a). In order to locate the indentations using X-ray, square platinum markers were then deposited at the corresponding array centers using a focused ion beam (FIB), and the size of the markers are 5μm, 5μm, 4μm, 3μm and 1.5μm for the 5 indentation depths from 3μm to 0.25μm, respectively.

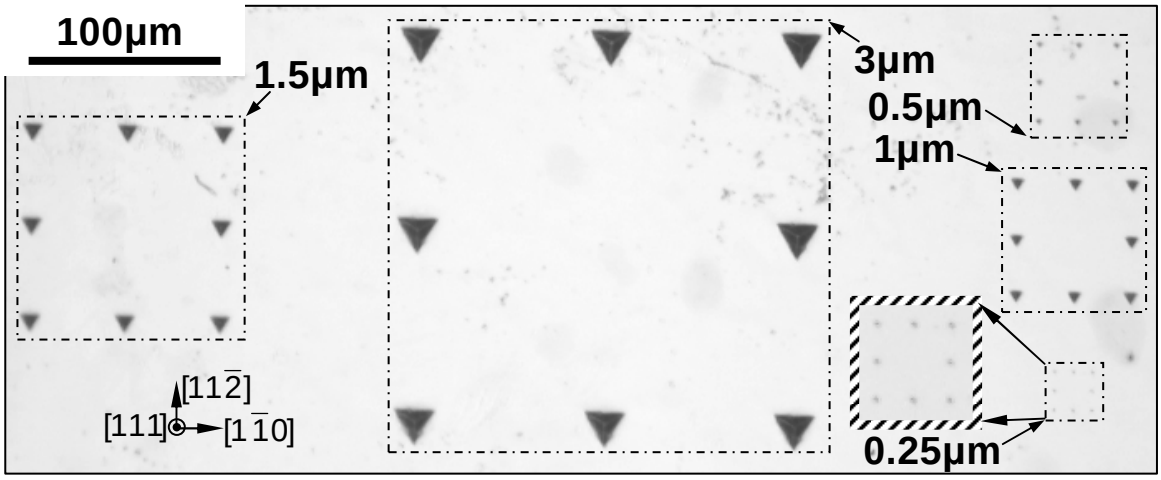

FIG. 1. An optical image of Berkovich indentation arrays on a single crystal (111) Cu with indentation depths ranging from 3 μm to 0.25 μm. Here, each of the labels from "3μm" to "0.25μm" indicates the indentation depth for the corresponding indentation array. This optical image is taken before depositing the Pt markers. Here, the inserted image bounded with thick shaded lines is a magnification of 2× for the corresponding 0.25μm indentation array.

The white beam X-ray microdiffraction (μXRD) experiment was performed on beamline 7.3.3. at the Advanced Light Source, Berkeley, CA. The sample was mounted on a precision XY Huber stage and oriented at an angle of 45° with respect to the incident beam (see Fig. 2(b)). Firstly, the indented sample surface was raster scanned at room

temperature under the X-ray beam to provide X-ray micro-fluorescence (μXRF), which revealed the Pt markers on the Cu sample to locate the indentation arrays. Then, finer μXRD scanning was conducted on the individual indents using a constant 0.8μm beam size (namely, full width at half maximum (FWHM) of the focused beam intensity is equal to about 0.8μm). As with typical synchrotron experiments, the scanning quantity and quality (resolution) were always balanced against the limited beam time. Only the 3μm, 1μm and 0.25μm indents were μXRD scanned with step sizes of 2μm, 1μm and 0.5μm, respectively. For each indentation depth, we scanned 3 individual indentations. The μXRD patterns were collected using a MAR133 X-ray charge-coupled device (CCD) detector and analyzed using the XMAS (X-ray microdiffraction analysis software) software package.[32] For the same experimental setup as shown in Fig. 2(b), Yang et al found that,[35-37] even after penetrating a copper sample as deep as 30~50μm, the incident beam can still generate detectable diffracted beams, indicating that the effective penetration length of X-ray microbeam for copper is at least 30~50μm.

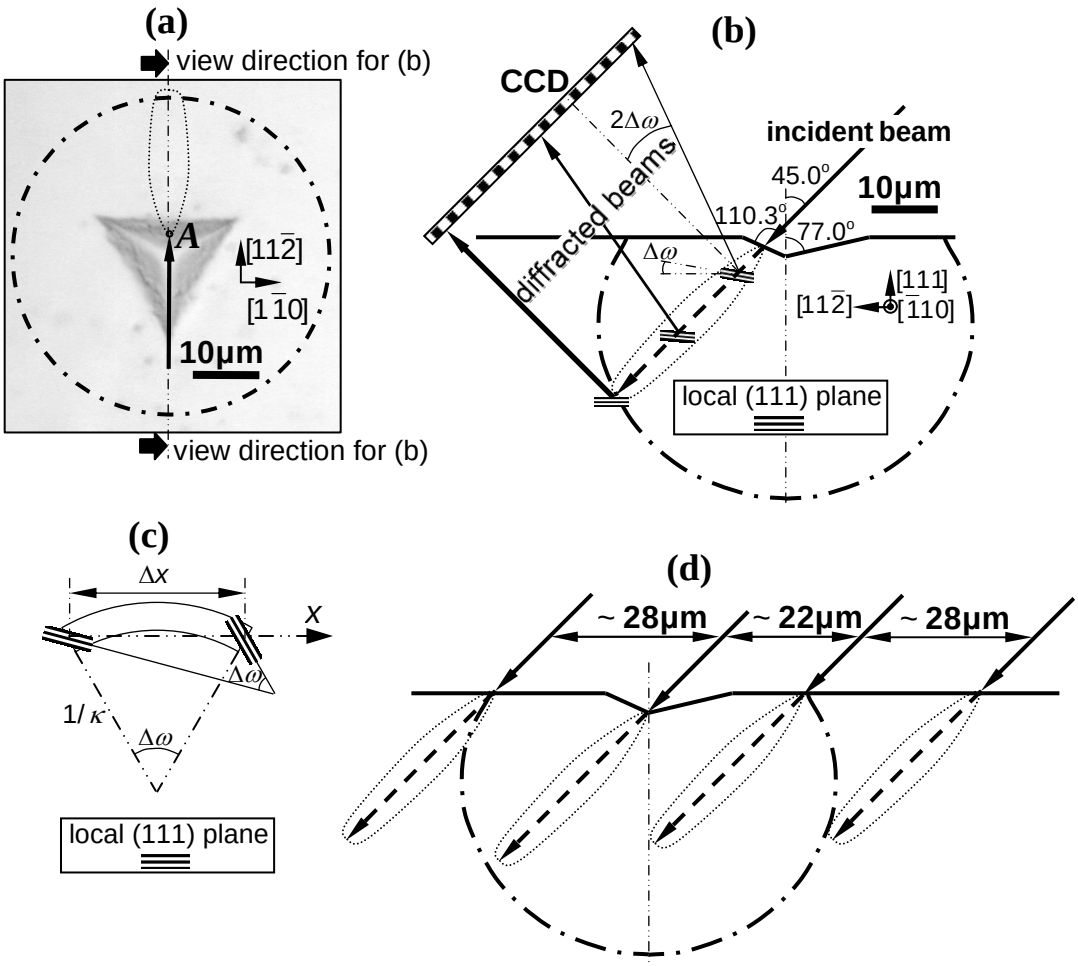

FIG. 2. The experimental setup for μXRD following the methodology by Yang et al.[35,36] (a) The optical image of a 3μm-deep indentation, showing that an indent edge was aligned with the $[1\bar{1}0]$ of the Cu single crystal, where position *A* is the center of the corresponding indent side face. (b) The schematic illustrating the cross-section of (a) on the plane containing both the incident beam at position *A* and the diffracted beams, where $\Delta\omega$ represents the local lattice rotation with respect to the undeformed lattice. (c) The schematic of lattice curvature. (d) The schematic of X-ray beam scanning showing the non-symmetry in the volumes probed by X-ray. Here, in (a), (b) and (d), thick dash-dot lines replicate the plastic zone boundary corresponding to 0.2% plastic strain contour determined by Finite Element Analysis (FEA) (see Fig. 8(b)), while

the thin dot lines schematically represent the volumes probed by the X-rays with an effective 30μm X-ray penetration length.

III. RESULTS & DISCUSSION

A. Mapping of Laue Peaks on the Area Covering an Individual Indent

We first describe the μSXRD map of an individual 3μm indentation with the incident beam scanning the indented and surrounding areas as in Fig. 3. The effective scanning step in the map, namely the distance between images, is 4μm, and each image in the map is the (111) Laue spot for the corresponding location scanned. Here, each image represents a two-dimensional (2D) diffraction intensity contour in the diffractometer χ-θ coordinates. Although the CCD detector records χ-2θ as illustrated in Fig. 2(b), the XMAS software processes the original CCD data and produces χ-θ plots; thus, in the following, the μSXRD results always refer to the χ-θ coordinates. In Fig. 3, the triangle represents the (Berkovich) indented area; the inner circle represents the equivalent circular contact area with a radius equal to a, while the outer dash-dot circle represents the simulated plastic zone boundary at the sample surface as in Figs. 2(a) and 2(b). For this 3μm deep indentation, a≈8.4μm, and the radius of the plastic zone boundary at the surface is about 3a, namely about 25μm. It should be noticed that, even at an X-ray-probed (X-ray-entering) position which is outside the plastic zone boundary at the surface, X-rays may still be able to probe the plastic zone due to the deep X-ray penetration as indicated in Fig. 2(d). In fact, Fig. 2(d) also indicates that, if the X-ray

penetration length can be known precisely, the μSXRD map as shown in Fig. 3 may be used to determine the size and the shape of a plastic zone.

For the regions far away from any indents (not shown in Fig. 3), the (111) Laue spots are circular without directional streaking, similar to the Laue spot at the lower right corner in Fig. 3. On the other hand, Fig. 3 shows various types and different extents of streaking in Laue spots, indicating the complexity of indentation-induced deformation. In order to determine the total indentation-induced lattice rotation, we should probe the X-ray microbeam within the indent (the triangle region in Fig. 3) as illustrated in Fig. 2(d). Furthermore, Fig. 3 shows that the Laue spot in position *A* involves a single directional streaking, indicating that, among all positions within the triangular indent, the lattice rotation corresponding to position *A* may be the simplest and cleanest for analysis. In fact, the Laue spots corresponding to positions *A* and *B* (see Figs. 3-4) are similar to those observed by Ice's group.[35,36] Through theoretical analysis and simulation,[39] Ice's group found that the X-ray probed volume at position *A* involves one rotation axis ($[1\bar{1}0]$) corresponding to two equally operating slip systems $(11\bar{1})[\bar{1}0\bar{1}]$ and $(11\bar{1})[0\bar{1}\bar{1}]$, representing the deformation associated with the corresponding indent side face. Here, the corresponding slip systems and the rotation axis can be easily understood through Fig. 4(b). On the other hand, the probed volume at position *B* involves multiple rotation axes. By using spatially resolved 3D X-ray structural microscopy, Ice's group could study the depth-profile of the rotation axis, and they found the following change of rotation axis along the X-ray penetration corresponding to position *B*:[35,36] $[01\bar{1}]$ close to the surface (note: $[10\bar{1}]$ was addressed in Ref. 35, which should be $[01\bar{1}]$ as personally communicated with the first author of Ref. 35), then several sequential transition axes,

and finally $[1\bar{1}0]$. This change of rotation axis can be understood by the comparison of Figs. 4(a) and 4(b) and explained as follows. For position *B*, the deformation close to the surface is dominated by the deformation induced by the side face *B*, so that the slip systems are $(\bar{1}11)[\bar{1}0\bar{1}]$ and $(\bar{1}11)[\bar{1}\bar{1}0]$ with an effective rotation axis of $[01\bar{1}]$. Then, for a deeper penetration of X-ray (see Fig. 4(a)), the deformation induced by side face *A* significantly contributes to the total deformation as well, so that the total effective rotation axis may be a convolution of the rotation axes $[1\bar{1}0]$ for face *A* and $[01\bar{1}]$ for face *B*, and the total effective rotation axis would change along the X-ray penetration due to the different degrees of sequential rotation around $[1\bar{1}0]$ and $[01\bar{1}]$. Finally, for deep enough X-ray penetration, the deformation induced by side face *A* would be dominant, so that the rotation axis becomes $[1\bar{1}0]$.

Thus, since the Laue streaking is the simplest at position *A*, for simplicity, all of our following attention will be focused on the streaked diffraction spots corresponding to position *A* for all indents studied.

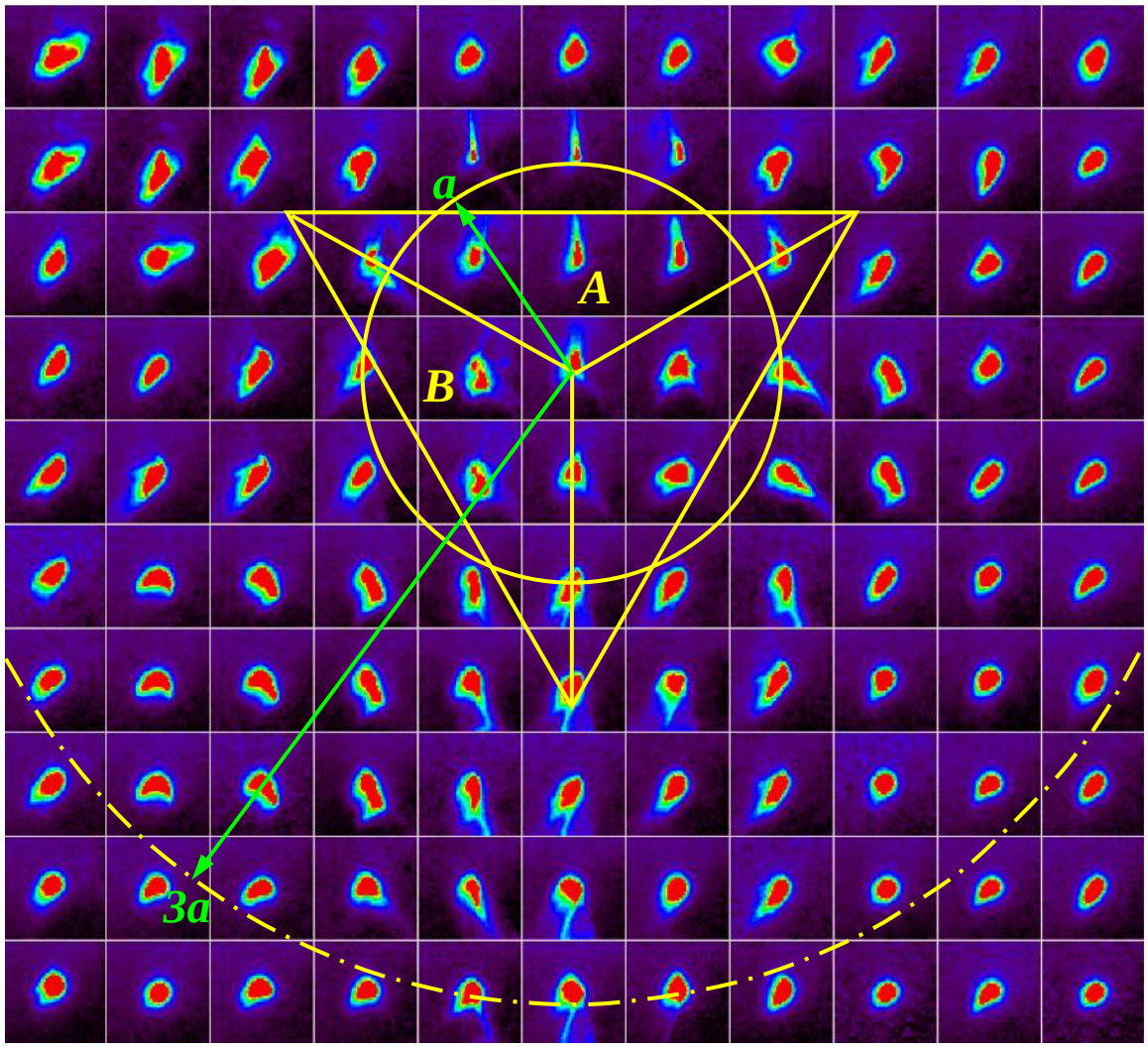

FIG. 3. 40×40μm^2 mapping of (111) Laue spots for different locations on the indented area of a 3μm indentation as well as areas surrounding it. Here, every image in the map is a 2D diffraction intensity contour plot with χ and θ as the horizontal and vertical coordinates, respectively, and the width ($\Delta\chi$) and height ($\Delta\theta$) of each image are 13.5^o and 14.5^o, respectively. Distance between images in this map is 4 μm (twice the 2μm step size for clarity). The triangle is the schematic of the Berkovich indent; the inner circle is the equivalent contact circle with a radius a, while the outer circle is the finite element analysis (FEA) determined plastic zone boundary at the surface with a radius about 3a (see Fig. 8(b)). Here, "*A*" and "*B*" denote the two positions which have been studied by Yang et al.[35,36]

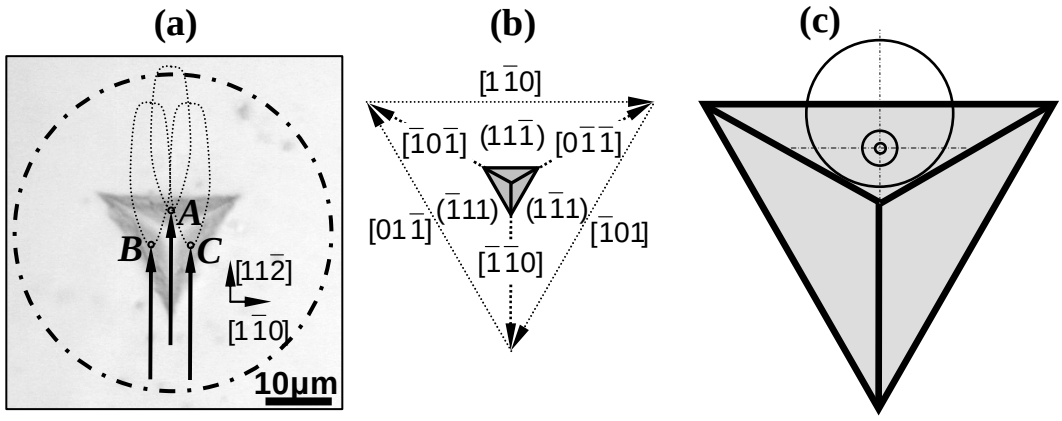

FIG. 4. (a)-(b) The comparison of a Berkovich indentation and the corresponding slip systems. (a) The same optical image as in Fig. 2(a), schematically showing the probed volumes corresponding to positions *A*, *B*, and *C*, respectively, where positions *A*, *B*, and *C* are the centers of the corresponding indent side faces *A*, *B* and *C*, respectively. (b) The projection of the slip systems into the indented (111) plane. Here, each indent side face mainly activates two slip systems which can be directly read from the corresponding part of (b), for instance, $(1\bar{1}1)[\bar{1}\bar{1}0]$ and $(1\bar{1}1)[0\bar{1}\bar{1}]$ for face *C*. In (b), the triangle (with thick solid black edges) represents a Berkovich indentation. Moreover, the rotation axis for each indent side face can also be directly read from (b), which is parallel to the corresponding indent edge, for instance, $[\bar{1}01]$ for face *C*. (c) The relative X-ray beam sizes compared to the corresponding indents; the 3 circles from the smallest to the largest represent the relative beam sizes corresponding to 3μm, 1μm, and 0.25μm indentations, respectively (for easy illustration, the indents of 3 different indentation depths are scaled to be the same, and the constant beam sizes are accordingly scaled to be different).

B. Comparison of Laue Peak Streaking for Different Indentation Depths

For each of the three indentation depths analyzed (3μm, 1μm and 0.25μm), we selected the particular (111) Laue diffraction spots coming from position *A* (we had three data sets for each indentation depth), and analyzed one representative diffraction spot for each indentation depth as shown in Figs. 5(a)-5(e). Here, Fig. 4(c) shows the relative X-ray beam sizes compared to the corresponding indents.

It should be mentioned that, as shown in Fig. 5(f) which is a landscape view of Fig. 5(c), there is some anomalous (extra diffraction) intensity at $\Delta\theta \approx 15°$ away from the main (111) Laue peak, and this anomalous intensity is not observable for the 1μm and 3μm indentations (not shown here). We think this anomalous intensity could be an artifact as the background residue due to surface scattering after the routine background removal, and this conclusion is based on the following observations and the related arguments. Firstly, because of our experimental setup as shown in Fig. 2(a), there is a very strong broad background scattering (reflection) centered exactly around the location (in χ-θ) where the anomalous intensity appears, and the background scattering would be normally removed through the routine background removal; however, if there are some irregular surface scattering from an imperfectly flat sample surface, some background residue might be left after the routine background removal. Secondly, in fact, Fig. 5(g) shows a similar anomalous intensity at the same position (in χ-θ), which is corresponding to another spatial position (rather than position *A*) around the same 0.25μm indentation, indicating that this anomalous intensity is not uniquely corresponding to the position *A*

for the indentation. Finally and most importantly, if this anomalous intensity resulted from a real lattice rotation due to deformation, a similar anomalous intensity associated with each of other (*hkl*) Laue peaks would appear in the Laue pattern, which is not the case for this particular anomalous intensity in question as shown in Figs. 5(f) and 5(g); on the other hand, as shown in Fig. 5(g), there is a *L*-shape intensity tail associated with the (111) Laue peak, which can be also seen from (224), (204), (202), and (313) peaks, indicating that this *L*-shape intensity tail is due to a real lattice rotation. Therefore, we can conclude that this anomalous intensity close to the (111) peak as shown in Fig. 5(f) is very probably an artifact as the background residue coming from the sample surface reflection. Thus, as shown in Fig. 5(c), for the 0.25μm indentation, we analyzed only the associated main (111) Laue peak excluding the anomalous intensity.

Figures 5(a)-5(e) show the streaked Laue diffraction spots and the intensity profiles along the corresponding streaking directions (dashed lines in the contour plots). Figures 5(a)-5(c) show that the streaking directions are at a small angle from the vertical direction, namely, $\Delta\chi \neq 0$, which may be due to the slight misalignment of the incident beam with respect to the proposed direction as illustrated in Figs. 2(a) and 2(b). In fact, the μXRD scanning for the 3μm and 0.25μm indents were done with the same sample stage setting, so that they correspond to the same streaking off-angle as in Figs. 5(a) and 5(c), whereas the μXRD scanning for the 1μm indent has a different streaking off-angle as in Fig. 5(b) due to the detaching and re-attaching of the sample to the sample stage.

Figures 5(a)-5(e) also shows that the shapes and extents of Laue streaking are very similar for the three different indentation depths, although it seems that a smaller indentation depth corresponds to a slightly larger streaking. Here, since the streaking off-

angles are small, for simplicity, the lattice rotation $\Delta\omega$ (see Fig. 2(b)) may be approximated by the extent of Laue streaking measured along the streaking direction (dash lines in Figs. 5(a)-5(c)). Using 1% of the maximum intensity as the threshold, Fig. 5(e) indicates that the Laue streakings ($\approx\Delta\omega$) for the indentation depths of 3μm, 1μm and 0.25μm are 4.6°, 6.5°, and 5.5°, respectively, which could be used to determine the strain gradients, or equivalently ρ_G as discussed below.

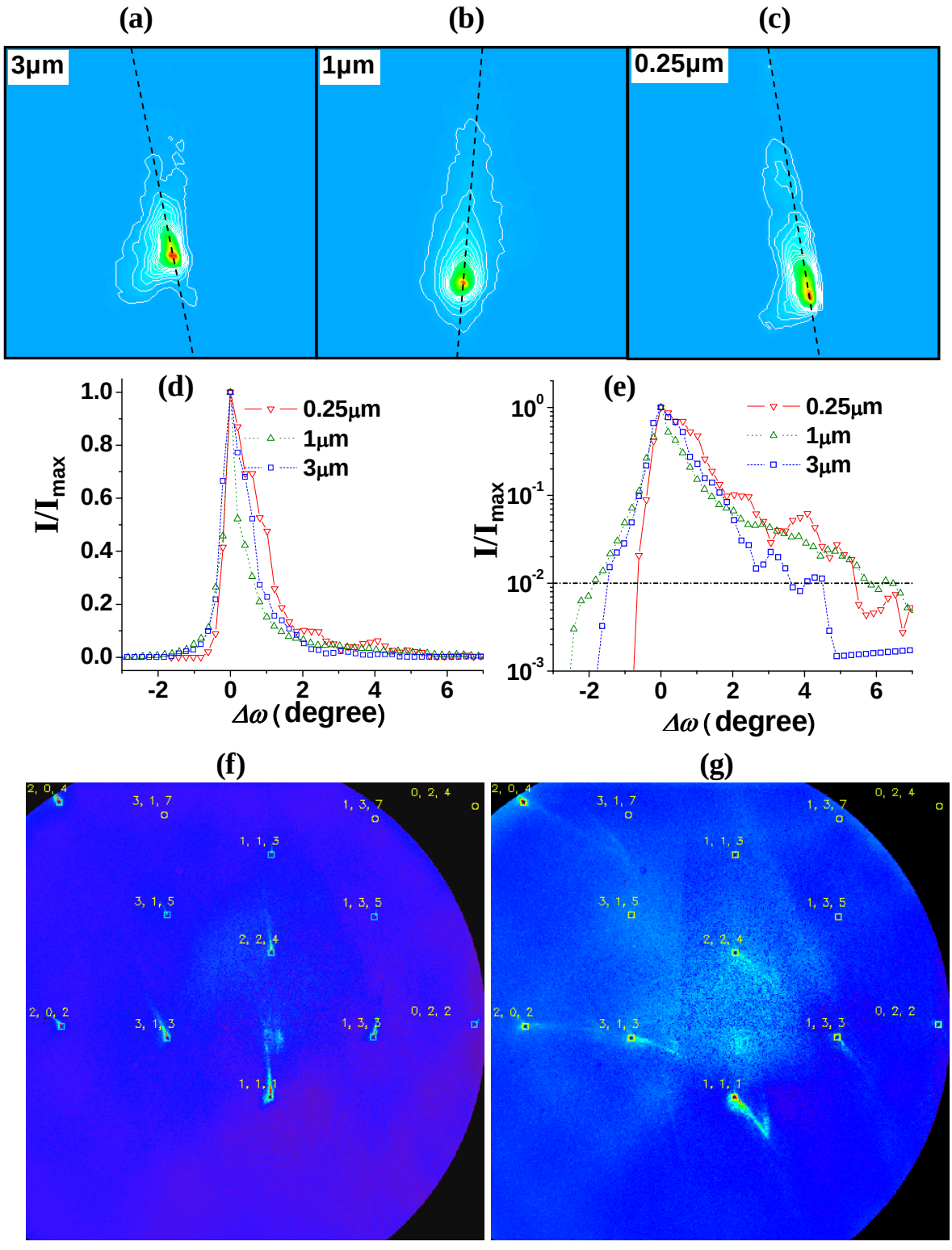

FIG. 5. (a)-(e) The Laue streakings for the representative (111) Laue diffraction peaks from position *A* corresponding to 3μm, 1μm, and 0.25μm indentation depths. (a)-(c) 2D rainbow

diffraction intensity contour plots in χ-θ coordinate (10.8°×10.8°) for the 3 indents;[41] here, the diffraction intensity is normalized by its corresponding maximum intensity, and the white contour lines (2.5%/contour) represent the normalized intensity from 1% to 21%. (d) The corresponding intensity profiles along the dashed lines in (a)-(c), respectively. (e) The Log-Linear plot of (d) with the 1% threshold. (f) The representative Laue pattern (a landscape view of (c)) for the same 0.25μm indentation. (g) The Laue pattern from another position (not *A*) around the same 0.25μm indentation.

C. The Relationship between the Laue Peak Streaking and the GND Density

In this section, we derive the essential equations for predicting ρ_G through μXRD data. As illustrated in Fig. 2(c), the relationship between lattice rotation ($\Delta\omega$) and lattice curvature (κ) can be approximated by[31,33,34,42]

$$\kappa = \frac{\partial \omega}{\partial x} \approx \frac{\Delta \omega}{\Delta x}, \tag{1}$$

where $\partial\omega/\partial x$ is the strain gradient, and Δx is the transition distance along x between the two viewing locations (see Fig. 2(c)). Here, the extent of Laue streaking is a direct measure of $\Delta\omega$ as discussed in the previous section; although it is obvious that the beam direction is the x direction, it is difficult to precisely determine Δx associated with the Laue streaking $\Delta\omega$. Since the lattice rotation due to elastic deformation is generally negligible compared to that due to plasticity, as a first order estimation, as illustrated in Fig. 2(b), Δx may be approximated by the size of the plastic zone in the case that the incident beam can penetrate the entire plastic zone. As mentioned before, the X-ray

penetration length is over 30-50μm, which is large enough for X-rays to penetrate the entire plastic zone of the 3μm indentation as shown in Fig. 2(b). Thus, for all indentation depths studied, Δx can be estimated by the corresponding plastic zone size. Moreover, as indicated in Fig. 2(b), the plastic zone could be approximated by an equivalent hemisphere with the center at the surface. Thus, by taking β as the ratio of the plastic zone radius to the equivalent contact radius (a), we have $\Delta x \approx \beta a$.

The relationship between the lattice curvature (κ) and the GND density (ρ_G) associated with that curvature is[31]

$$\rho_G = \frac{\kappa}{b_x} = \frac{\partial \omega}{\partial x}\frac{1}{b_x}, \tag{2}$$

where b_x is the component of the dislocation Burgers vector projected onto the transition direction (the x direction) shown in Fig. 2(c). Combining Eqs. 1 and 2, and noticing $\Delta x \approx \beta a$, we get

$$\rho_G \approx \frac{\Delta \omega}{b_x \beta a} \approx \frac{\Delta \omega}{b_x \beta h \tan \alpha}, \tag{3}$$

where α is the semi-angle (70.3°) of the Berkovich-equivalent conical indenter. To derive Eq. 3, since the indentation sink-in is small as indicated in Fig. 2(a), we neglect the difference between the contact indentation depth and the total indentation depth.

It should be noticed that, for the case of indentation, the strain gradient, i.e. $\partial \omega / \partial x$, decreases rapidly from the indented surface into the sample, i.e. along the X-ray penetration (the x direction);[13,35,36,43] thus, Eq. 2 indicates that ρ_G is not a constant but rapidly decreases along the line of penetration. Thus, Eq. 3 is only an estimation of the average GND density. The determination of the dimensionless plastic zone size (β) is essential to estimate ρ_G using Eq. 3, which will be discussed below.

D. The Relationship between the Indentation Data and the GND Density

Figure 6 shows the indentation data for a 3μm indentation and also two corresponding finite element analysis (FEA) simulations. Here, the continuous stiffness measurement (CSM) module in Nanoindenter XP^{TM} can continuously record the contact stiffness during an indentation, so that the hardness depth profile can be obtained through a single indentation as shown in Fig. 6(b). There were 8 data sets for 3μm indentations (see Fig. 1); since all 8 data sets overlap each other nearly perfectly (not shown here), we did the analysis for a representative one, as shown in Fig. 6. Fig. 2(a) indicates that the indent shows a slight sink-in, which is consistent with the fact that the sample is an annealed good quality crystal,[44,45] indicating that the Cu crystal may exhibit significant strain-hardening.[44,45] In order to eliminate any uncertainties due to the sink-in effect, surface roughness, and area function of the indenter, we calculated the "true" hardness as shown in Fig. 6(b) based on the continuously measured contact stiffness and by inputting the following elastic properties of Cu: Young's modulus E=120.5GPa, and Poissons' ratio ν =0.35; the details of calculating the "true" hardness are described in Ref. 46.[46] Fig. 6(b) clearly shows the indentation-depth-dependent hardness (smaller is harder), i.e. the indentation size effect (ISE). It should be noticed that there is a softening phenomenon for indentation depth less than 250nm, which might be due to the non-self-similar expansion of plastic zone and/or the tip bluntness,[43,46] and this softening phenomenon was also observed for single crystal Ni and Cu by other researchers.[18,47]

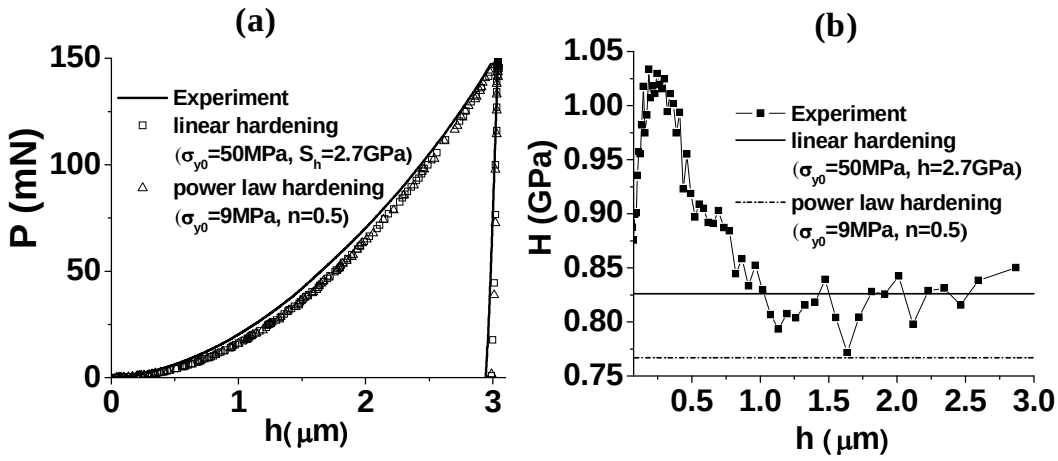

FIG. 6. (a) The indentation load (P) vs. the indentation depth (h) plot for a 3μm indentation and also two corresponding FEA simulations, where σ_{y0} is the yield strength, S_h is the strain hardening rate of linear hardening, and n is the power of power law hardening. (b) The corresponding Hardness (H) vs. the indentation depth (h) plot for (a).

Following the work of Stelmashenko et al[4] and De Guzman et al,[5] Nix and Gao[8] provided a simple explanation for this depth-dependent hardness, in terms of the geometrically necessary dislocation (GND) density as a function of indentation depth. Durst and Goken[16] as well as Feng[17] later modified the model to account primarily for the fact that the plastic zone radius is not equal to the contact radius, as Nix and Gao had assumed. Still the revised model takes the form:

$$\frac{H}{H_0} = \sqrt{1 + \frac{h_0}{h}}, \tag{4}$$

which can also be expressed equivalently as:

$$\frac{H}{H_0} = \sqrt{1 + \frac{\rho_G}{\rho_S}}, \tag{5}$$

where $$\rho_S = \frac{H_0^2}{M^2 C_H^2 \alpha_t^2 \mu^2 b^2} = \frac{1.5\cot^2\alpha}{\beta^3 b_n}\frac{1}{h_0}. \quad (6)$$

H_0 is the limit of the hardness when the indentation depth becomes indefinitely large ($h\to\infty$), and h_0 is a material length scale. In Eq. 6, ρ_S is the density of statistically stored dislocations (SSDs); M is the Taylor factor, and M=3.06 for face center cubic (FCC) materials;[9,43] C_H is the ratio of H_0 to the effective flow stress (σ_{ye}) corresponding to an indefinitely large indentation; α_t is the Taylor constant, and it in the range of 0.2~0.5 for FCC metals;[8,10,31] μ is the shear modulus; b is the magnitude of the Burgers vector, and b_n is the component of the Burgers vector projected onto the normal axis ([111] here) of the indented sample surface; α is the semi-angle (70.3°) of the Berkovich-equivalent conical indenter, and β is the ratio of the plastic zone size to the contact radius. To derive Eq. 6, as indicated in Figs. 2(a) and 6(a), we have neglected the differences among the residual indentation depth, the contact depth, and the maximum indentation depth. Here, ρ_S is the dislocation density corresponding to the local plastic strain, and ρ_G is the excess dislocation (GND) density corresponding to the local gradient of plastic strain.[31] It should be noticed that, although both ρ_S and ρ_G can be defined locally, ρ_S and ρ_G in Eqs. 3, 5, and 6 are referred as the average values of the corresponding densities throughout the plastic zone.

Equation 4 implies that the square of H has a linear relationship with $1/h$, as shown in Fig. 7.

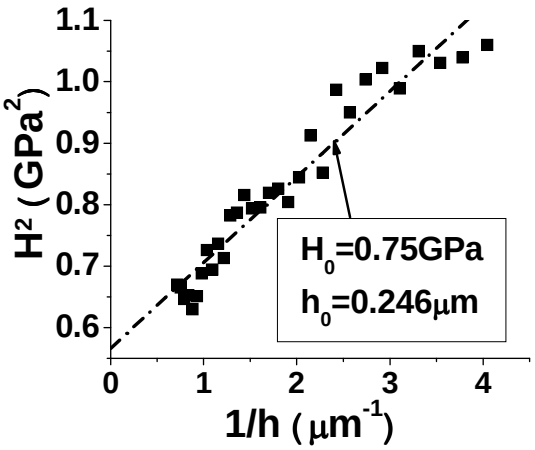

FIG. 7. The H^2 vs. $1/h$ plot for the experimental data in Fig. 6(b). Here the square symbol represents the experimental data for h>250nm, and the dash-dot line represents the fitting result using Eq. 4.

Because the average SSD density (ρ_S) is nominally independent of indentation depth,[8] the indentation-depth-dependent hardness (see Fig. 7) implies an indentation-depth-dependent average GND density (ρ_G), or equivalently, an indentation-depth-dependent average strain gradient ($\Delta\omega/\Delta x$) (see Eqs. 1-3). By rearranging Eqs. 4-6, we can express ρ_G in different ways:

$$\rho_G = \frac{H_0^2}{M^2 C_H^2 \alpha_t^2 \mu^2 b^2} \frac{h_0}{h}, \tag{7a}$$

$$\rho_G = \frac{H_0^2}{M^2 C_H^2 \alpha_t^2 \mu^2 b^2} \left(\frac{H^2}{H_0^2} - 1 \right), \tag{7b}$$

$$\rho_G = \frac{1.5 \cot^2 \alpha}{\beta^3 b_n} \frac{1}{h}. \tag{7c}$$

Equations 7(a) and 7(b) can be used to predict ρ_G as a function of h through the experimental hardness data. Eq. 7(c) is an interesting result, indicating that the product of

h and ρ_G is a constant which depends on the indenter geometry (α) and b_n, and the effect of material mechanical properties is indirectly represented only through the size of the plastic zone (β). The comparison between Eqs. 6 and 7(c) indicates that ρ_G increases with decreasing h and is equal to ρ_S at $h=h_0$. Moreover, according to Eqs. 2-3 and 7(c), by matching ρ_G, the average indentation-induced strain gradient ($\Delta\omega/\Delta x$) may be given by

$$\frac{\Delta\omega}{\Delta x} \approx \frac{1.5\cot^2\alpha}{\beta^3 h}\frac{b_x}{b_n} \approx \frac{1.5\cot^2\alpha}{\beta^3 h} = \frac{1.5\cot\alpha}{\beta^3 a}. \qquad (8a)$$

Equation 8(a) indicates that the average strain gradient ($\Delta\omega/\Delta x$) would be proportional to $1/h$ as expected, and that $\Delta\omega/\Delta x$ may depend on the probing direction (x) through the direction-dependence of b_x. Here, Eq. 8(a) is consistent with Nix and Gao's estimation,[8] namely, $\Delta\omega/\Delta x \approx \cot\alpha/a$, in which β is taken to be 1.0. Then, according to Eqs. 1-3 and 8(a), we have the following relation between the lattice rotation $\Delta\omega$, namely, the observed Laue streaking, and the plastic zone size (β) as

$$\Delta\omega \approx \frac{1.5\cot\alpha}{\beta^2}\frac{b_x}{b_n} \approx \frac{1.5\cot\alpha}{\beta^2}, \qquad (8b)$$

indicating that the lattice rotation $\Delta\omega$ may be independent of the indentation depth as roughly shown in Figs. 5(a)-5(e). Furthermore, Eq. 8(b) can be used to estimate β through the observed Laue streaking; thus, the average $\Delta\omega \approx 5.5^o$ for the 3 indentation depths as in Fig. 5 implies $\beta \approx 2.3$.

In addition, Eq. 6 provides the condition of model self-consistency, namely,

$$\frac{\beta^3}{C_H{}^2} = \frac{3M^2}{2}\frac{\mu^2 b}{H_0{}^2 h_0}\frac{b}{b_n}\frac{\alpha_t{}^2}{\tan^2\alpha} = 8.15\alpha_t{}^2. \qquad (9)$$

Here, based on the slip systems illustrated in Fig. 4(b), b_n/b=0.816. To derive Eq. 9, we have used the following values: M=3.06, μ=44.7GPa, b=0.256nm, α=70.3°, H_0=0.75GPa, h_0=246nm, and b_n=0.209nm. For FCC metals, α_t is in the range of 0.2~0.5.[8,10,31] By satisfying the condition of model self-consistency (Eq. 9), it is obvious that Eqs. 7(a)-7(c) are identical, so that we will use Eq. 7(c) in the following due to its simple form. In fact, the hardness data are not explicitly expressed in Eq. 7(c) but indirectly represented in the condition of model self-consistency (Eq. 9).

As indicated in Eqs. 3 and 7(c), in order to calculate ρ_G, β is the essential parameter. Although β and C_H for work-hardened metals may be well approximated by 1.9 and 2.6,[45,48,49] respectively, the corresponding values of β and C_H for annealed metals may be larger.[44,48] In the following section, we will first discuss the ways to estimate β, and then we will compare the two values of ρ_G calculated using Eqs. 3 and 7.

E. The Comparison of the Two Values of GND Density through Hardness and Laue Streaking

In order to have a better estimation of β, we performed finite element analysis (FEA) using the ABAQUS™ software package. The FEA results are shown in Figs. 6 and 8 as well as listed in Table I. Figure 6 indicates that the FEA simulations assuming both linear hardening and power-law hardening match the experimental results, and it should be noticed that our FEA simulations was based on conventional plasticity and did not include the extra hardening associated with strain gradients. As illustrated in Fig. 8, the ratio of the contact radius to the maximum depth is about 0.92 for both the hardening

laws, indicating a small sink-in effect, which is consistent with the shape of the residual indents as shown in Fig. 2(a). Although the strain-hardening property of our annealed copper sample was not experimentally tested, Lim and Chaudhri found that[50] the strain-hardening law for well annealed polycrystalline copper is power-law hardening with $n \approx 0.5$. Furthermore, Figs. 6 and 8 as well as Table I indicate that the two significantly different hardening laws (linear and power-law) give very similar results, implying a small effect of changing hardening laws. Therefore, we will estimate the quantities for our Cu sample using the averages of the corresponding FEA-computed values determined from the two hardening laws.

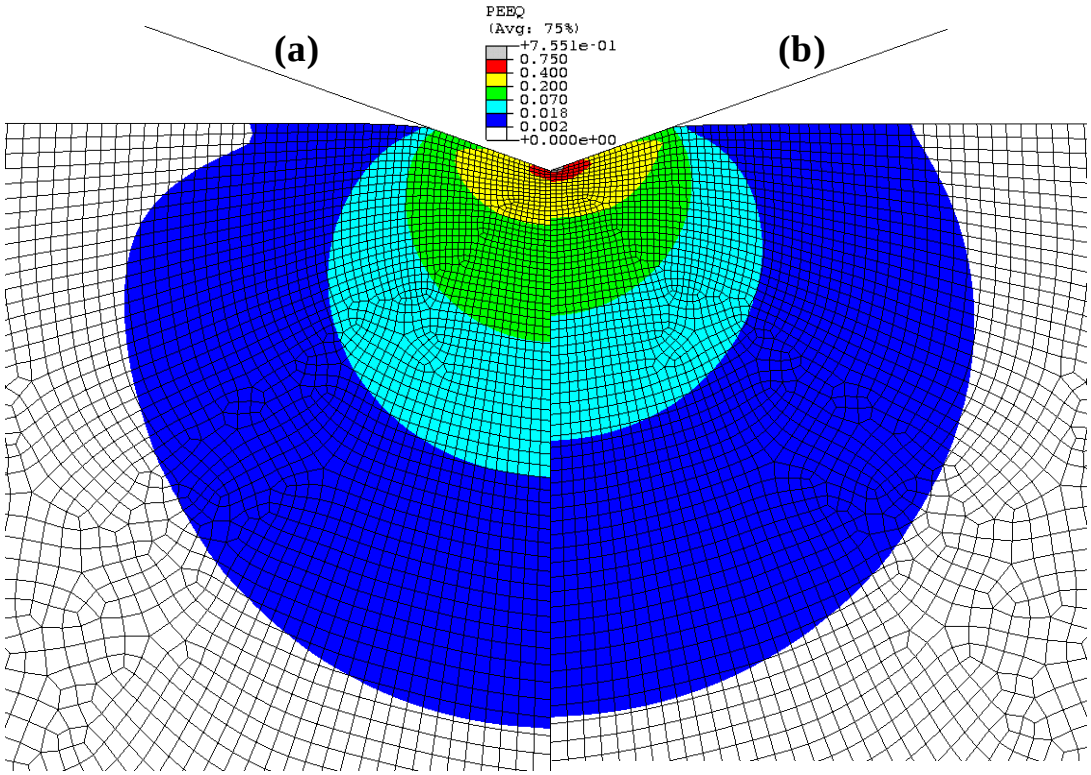

FIG. 8. The FEA-calculated equivalent plastic strain (PEEQ in ABAQUS^{TM}) contour plots. (a) For σ_{y0}=50MPa, S_h=2.7GPa/plastic strain, assuming linear strain hardening. (b) For σ_{y0}=9MPa,

n=0.5, assuming power-law hardening.[45] Here, the two images are scaled to have the same contact radius for a better comparison.

Since both Eqs. 3 and 7(c) are derived based on the averaging throughout the plastic zone, a representative quantity is needed for identifying the plastic zone boundary, and the equivalent plastic strain (ε_p) as in Fig. 8 may be a good candidate for the quantity. Figure 8 indicates that the indentation-induced plastic strain is highly non-uniform and concentrated below indentation. Consequently, there might be two kinds of effective plastic strain: one (ε_{pb}) for identifying the plastic zone boundary and the other one (ε_{pe}) equal to the average strain in the corresponding plastic zone; it is obvious $\varepsilon_{pe} >> \varepsilon_{pb}$ due to the highly strain concentration under indentation as in Fig. 8. In fact, the definition of the average strain ε_{pe} is consistent with that of the representative indentation plastic strain (ε_{pr}) which is a measure of the average indentation-induced plastic strain, and the ratio of hardness to the flow stress corresponding to ε_{pr} is equal to about 3.[48] Johnson suggested that $\varepsilon_{pr} \approx 0.2\tan\alpha$,[48] namely, $\varepsilon_{pr} \approx 7\%$ for a Berkovich indentation, which is consistent with the FEA results ($H/\sigma_y \approx 3.1$ at $\varepsilon_p \approx 7\%$) as listed in Table I. Thus, we should expect that the average strain $\varepsilon_{pe} \approx \varepsilon_{pr} \approx 7\%$ is much larger than the effective strain at the plastic boundary (ε_{pb}); the 7%-plastic-strain contour may be an inner bound for estimating the plastic zone boundary, whereas the 0.2%-plastic-strain contour may be expected to be an outer bound for the plastic zone boundary. By measuring the strain contours in Fig. 8 using Scion™ Image software, the 7% and 0.2% plastic-strain contours correspond to $\beta \approx 1.45$ and $\beta \approx 4.3$, respectively, as listed in Table I; thus, $\beta \approx 1.45$ and $\beta \approx 4.3$ may be the lower and upper

bounds for β, respectively. By inserting the estimated values of β, ρ_G can be calculated using Eq. 7(c) based on the revised Nix-Gao model and using Eq. 3 through μXRD data.

Figure 9 shows the comparison of the two values of ρ_G calculated using Eqs. 3 and 7(c). Here, b_x=0.781b=0.2nm, according to the corresponding slip systems (Fig. 4(b)) and the experimental setup (Fig. 2(b)). Figures 9(a) and 9(b) indicate that, by taking β = 1.45 (β = 4.3), ρ_G calculated using Eq. 7 is much larger (smaller) than that calculated using Eq. 3. This large difference between the two predictions can be understood by the large gradient of ρ_S due to the plastic strain concentration as shown in Fig. 8 and also the large gradient of ρ_G as indicated by the rapid decrease of strain gradient along the X-ray penetration path.[13,35,36,43] Moreover, as discussed above, β≈1.45 and β≈4.3 may be the lower and upper bounds for β, respectively; thus, as shown in Fig. 9(a), the over- or under-estimation of β would have a much larger effect through $\rho_G \propto 1/(\beta^3 h)$ (Eq. 7(c)) than through $\rho_G \propto 1/(\beta h)$ (Eq. 3).

As discussed in the previous section, based on Eq. 8(b) and the Laue streaking as in Fig. 5, β≈2.3. Alternatively, Figure 9 also shows that, if we take β≈2.3, i.e. ε_{pb} ≈1.8% (see Fig. 8 and Table I), the two estimates of ρ_G calculated from Eqs. 3 and 7(c) match nicely, implying that β ≈2.3 might be a nice estimation for the effective plastic zone size. In fact, this estimation of β (≈2.3) is consistent with Durst et al's estimation (β ≈2.2) through their study of the ISE in single crystal Cu and Ni.[18] Then, based on this estimation of β (≈2.3), ρ_G and ρ_S vs. h for the single crystal (111) Cu are plotted in Fig. 9(c); here, since h_0 ≈250nm, ρ_G ≈ρ_S (≈300μm^{-2}) at h=250nm. It should be noticed that, as discussed before, due to the strong plastic strain concentration, the effective plastic strain at the

plastic zone boundary ($\varepsilon_{pb}\approx 1.8\%$) << the average plastic strain in the plastic zone ($\varepsilon_{pe}\approx\varepsilon_{pr}\approx 7\%$).[48]

In the following, we want to discuss some implications of the previous results on strain gradient plasticity. According to a law for strain gradient plasticity theory,[10] we have

$$\left(\frac{\sigma}{\sigma_y}\right)^2 = 1+\hat{l}\eta\,, \tag{10}$$

where σ is the flow stress, σ_y is the flow stress in the absence of strain gradients, $\eta=\rho_G b$ is the strain gradient,[10] and $\hat{l}$ is a material length scale. Then, according to Eqs. 5, 6, and 10, noticing that $\eta=\rho_G b$ and $H\propto\sigma$, we have

$$\hat{l} = \frac{1}{\rho_S b}\,, \tag{11a}$$

$$\hat{l} = M^2\alpha_t^2\left(\frac{\mu}{\sigma_{ye}}\right)^2 b = \frac{\beta^3}{1.5}\frac{b_n}{b}\tan^2\alpha\; h_0\,. \tag{11b}$$

Equation 11(a) indicates that the material length scale $\hat{l}$ depends on ρ_S which is dependent on the average plastic strain level; thus, $\hat{l}$ is not a purely "intrinsic" material constant, and it also depends on the mode of deformation. For example, for an indentation problem, Eq. 11(b) indicates that $\hat{l}$ depends on the indentation-induced effective flow stress (σ_{ye}) corresponding to $h\to\infty$ or equivalently on the indentation-induced average plastic strain (ε_{pe}); alternatively, $\hat{l}$ depends on the material mechanical properties (indirectly through β) and also the indenter geometry (α). Then, by inputting the estimation of $\beta\approx 2.3$, Eq. 11(b) predicts that $\hat{l}\approx 13\mu$m for copper indented with a

Berkovich indenter. Moreover, by taking σ_{ye}≈252MPa corresponding to ε_{pe}≈ε_{pr}≈7% as listed in Table I, we have C_H ≈3.1, and Eq. 11(b) (equivalently the condition of model self-consistency (Eq. 9)) predicts that the Taylor constant α_t ≈0.4 for copper. Thus, based on Eqs. 8(b) and 9, using the indentation-depth-dependent hardness data (H_0 and h_0) and the corresponding μXRD data ($\Delta\omega$), we might obtain a way of estimating the Taylor constant α_t by

$$\alpha_t \approx \frac{1.1}{MC_H}\left(\frac{H_0^2 h_0}{\mu^2 b}\right)^{1/2}\left(\frac{b_x^3}{b_n b^2}\frac{\tan\alpha}{\Delta\omega^3}\right)^{1/4}. \qquad (12)$$

Here, as discussed above, the effective (average) indentation-induced flow stress (σ_{ye}) corresponds to ε_{pe}≈ε_{pr}≈7% rather than ε_{pe}=0% or 0.2%; thus, C_H (=H/σ_{ye}, i.e. ≠ H/σ_{y0}) can be estimated nicely by 3.0 for most materials except those with high yield-strength-to-modulus ratios.[48,49]

In summary, by matching ρ_G predicted by the revised Nix and Gao model and that determined through μXRD data, we find that the dimensionless indentation plastic zone size β≈2.3, which is corresponding to the 1.8%-plastic strain-contour determined through finite element analysis. Thus, the average SSD density (ρ_S) for a Berkovich indentation on (111) Cu single crystal is determined to be about 300μm^{-2}, corresponding to a mean distance between SSDs of ~58nm. Through indentation hardness and the corresponding μXRD data, we could estimate the material length scale ($\hat{l}$) for copper indented with a Berkovich indenter and also the Taylor constant (α_t) for copper: $\hat{l}$ ≈13μm and α_t ≈0.4.

TABLE I. The inputs and outputs of the FEA simulations[a)]

Strain-hardening Law	*Simulation inputs*			H *(GPa)*	h_c/h	ε_p *(%)*	σ_y *(MPa)*	H/σ_y	β
	σ_0 (MPa)	S_h (MPa)	*n*						
Linear	50	2700	-	0.821	0.92	0.2	55.4	14.8	4.3
						1.8	98.6	8.3	2.4
						7	239	3.4	1.5
Power-law	9	-	0.5	0.765	0.92	0.2	48.7	15.7	4.3
						1.8	136.6	5.6	2.2
						7	265	2.9	1.4
Average	-	-	-	0.793	0.92	0.2	52	15.3	4.3
						1.8	118	6.7	2.3
						7	252	3.1	1.45

a) Here, h_c is the indentation contact depth. σ_0 is the initial yield strength, S_h is the strain-hardening rate for linear strain hardening, and n is the power of power-law hardening. ε_p is the plastic strain, and σ_y is the corresponding flow stress. Each plastic zone radius (βa) is estimated by the radius of an equivalent circle with the area equal to 4 times of the region surrounded by the corresponding iso-plastic-strain contour as shown in Fig. 8(a) or Fig. 8(b), and the images were analyzed using Scion™ Image software.

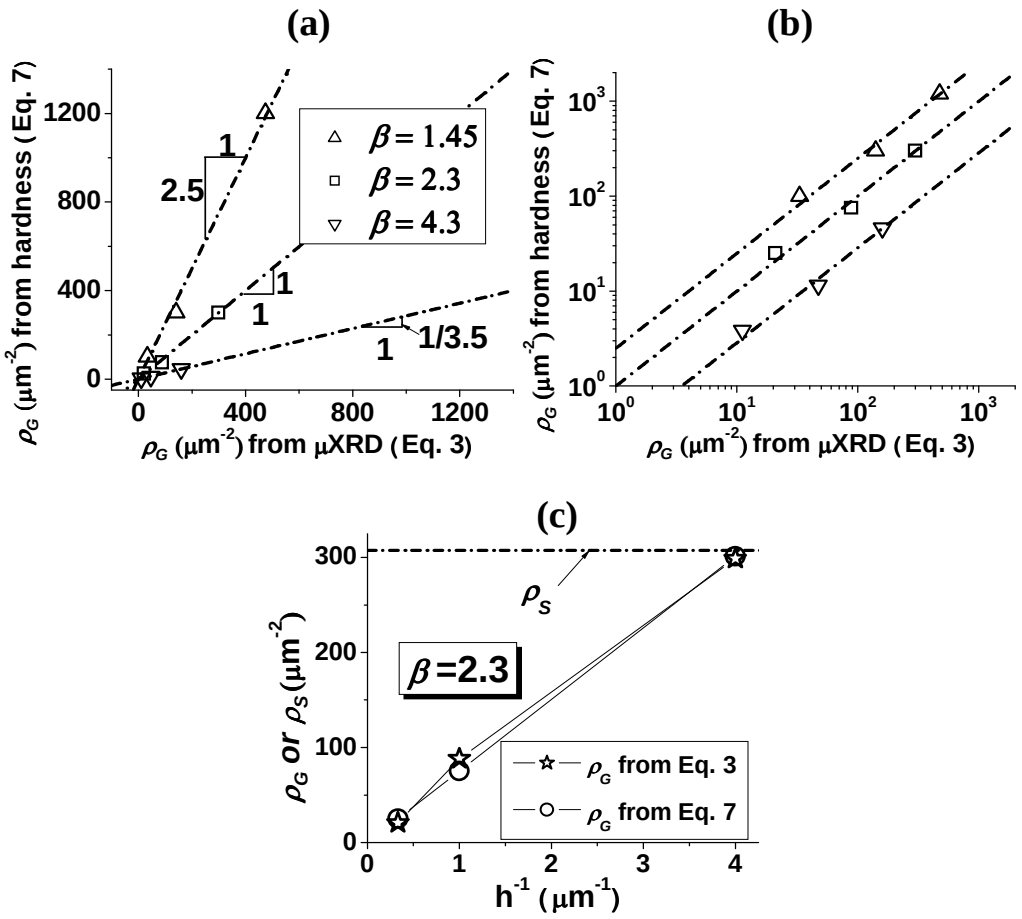

FIG. 9. The comparison of ρ_G calculated using Eqs. 3 and Eq. 7(c): (a) the linear-linear plot, (b) the corresponding Log-Log plot. Here, for (a) and (b), the upper triangle, square, and lower triangle symbols correspond to the plastic strain equal to 7%, 1.8%, and 0.2%, i.e. β = 1.45, 2.3, and 4.3, respectively. (c) The plot of dislocation densities vs. 1/*h* corresponding to β =2.3.

IV. CONCLUSION

Using a synchrotron technique involving white-beam X-ray microdiffraction (μXRD), we have observed Laue peak streaking near small indentations in the (111) surface of a copper single crystal. The geometrically necessary dislocation density, $\rho_{G,}$

computed from the observed streaking increases with decreasing indentation depth, which is in good agreement with ρ_G computed from the observed indentation size effect (ISE) using a revised Nix-Gao model. This finding supports that the ISE is associated with geometrically necessary dislocations and related strain gradients. Moreover, it is demonstrated that μXRD is a good tool for probing the deformation mechanism at the sub-micrometer scale.

ACKNOWLEDGMENTS

This work was supported by the Office of Science, Office of Basic Energy Sciences, of the U.S. Department of Energy under Contract No. DE-FG02-04ER46163. Additional support through an NSF-EU COLLABORATIVE RESEARCH PROGRAM: NANOMESO under NSF Grant No. 0502208 is gratefully acknowledged. The Advanced Light Source (ALS) is supported by the Director, Office of Science, Office of Basic Energy Sciences, of the U.S. Department of Energy under Contract No. DE-AC02-05CH11231 at the Ernest Orlando Lawrence Berkeley National Laboratory (LBNL). Prof. Wendelin J. Wright at Santa Clara University and Dr. Ann Marshall at Stanford University are acknowledged for helping with the deposition of Pt markers.

[1] E. Arzt, Acta Materialia **46,** 5611-5626 (1998).

[2] D. Y. W. Yu and F. Spaepen, Journal of Applied Physics **95,** 2991-2997 (2004).

[3] W. D. Nix, Metallurgical Transactions a-Physical Metallurgy and Materials Science **20,** 2217-2245 (1989).

[4] N. A. Stelmashenko, M. G. Walls, L. M. Brown, and Y. V. Milman, Acta Metallurgica Et Materialia **41,** 2855-2865 (1993).

[5] M. S. De Guzman, G. Neubauer, P. Flinn, and W. D. Nix, Materials Research Society Symposium - Proceedings **308,** 613-618 (1993).

[6] Q. Ma and D. R. Clarke, Journal of Materials Research **10,** 853-863 (1995).

[7] W. J. Poole, M. F. Ashby, and N. A. Fleck, Scripta Materialia **34,** 559-564 (1996).

[8] W. D. Nix and H. J. Gao, Journal of the Mechanics and Physics of Solids **46,** 411-425 (1998).

[9] H. Gao, Y. Huang, and W. D. Nix, Naturwissenschaften **86,** 507-515 (1999).

[10] H. Gao, Y. Huang, W. D. Nix, and J. W. Hutchinson, Journal of the Mechanics and Physics of Solids **47,** 1239-1263 (1999).

[11] Y. Huang, J. Y. Chen, T. F. Guo, L. Zhang, and K. C. Huang, International Journal of Fracture **100,** 1-27 (1999).

[12] Y. Huang, H. Gao, W. D. Nix, and J. W. Hutchinson, Journal of the Mechanics and Physics of Solids **48,** 99-128 (2000).

[13] Y. Huang, Z. Xue, H. Gao, W. D. Nix, and Z. C. Xia, Journal of Materials Research **15,** 1786-1796 (2000).

[14] N. I. Tymiak, D. E. Kramer, D. F. Bahr, T. J. Wyrobek, and W. W. Gerberich, Acta Materialia **49,** 1021-1034 (2001).

[15] J. G. Swadener, E. P. George, and G. M. Pharr, Journal of the Mechanics and Physics of Solids **50,** 681-694 (2002).

[16] K. Durst, B. Backes, and M. Goken, Scripta Materialia **52,** 1093-1097 (2005).

[17] G. Feng, Ph.D. Thesis, Stanford University, 2005.

[18] K. Durst, B. Backes, O. Franke, and M. Goken, Acta Materialia **54,** 2547-2555 (2006).

[19] S. J. Basinski and Z. S. Basinski, in *Dislocations in solids*; *Vol. 4*, edited by F. R. N. Nabarro (North-Holland Publishing Company, Oxford, UK, 1979), p. 261-362.

[20] M. R. Castell, A. Howie, D. D. Perovic, D. A. Ritchie, A. C. Churchill, and G. A. C. Jones, Philosophical Magazine Letters **67,** 89-93 (1993).

[21] P. E. Donovan, Journal of Materials Science **24,** 523-535 (1989).

[22] R. Hill, E. H. Lee, and S. J. Tupper, Proceedings of the Royal Society of London. Series A, Mathematical and Physical Sciences **188,** 273-289 (1947).

[23] T. O. Mulhearn, Journal of the Mechanics and Physics of Solids **7,** 85-96 (1959).

[24] B. J. Inkson, T. Steer, G. Mobus, and T. Wagner, Journal of Microscopy-Oxford **201,** 256-269 (2001).

[25] T. Y. Tsui, J. Vlassak, and W. D. Nix, Journal of Materials Research **14,** 2196-2203 (1999).

[26] T. Y. Tsui, J. Vlassak, and W. D. Nix, Journal of Materials Research **14,** 2204-2209 (1999).

[27] D. Kiener, R. Pippan, C. Motz, and H. Kreuzer, Acta Materialia **54,** 2801-2811 (2006).

[28] N. Zaafarani, D. Raabe, R. N. Singh, F. Roters, and S. Zaefferer, Acta Materialia **54,** 1863-1876 (2006).

[29] G. B. Viswanathan, E. Lee, D. M. Maher, S. Banerjee, and H. L. Fraser, Acta Materialia **53,** 5101-5115 (2005).

[30] S. J. Lloyd, A. Castellero, F. Giuliani, Y. Long, K. K. McLaughlin, J. M. Molina-Aldareguia, N. A. Stelmashenko, L. J. Vandeperre, and W. J. Clegg, Proceedings of the Royal Society a-Mathematical Physical and Engineering Sciences **461,** 2521-2543 (2005).

[31] N. A. Fleck, G. M. Muller, M. F. Ashby, and J. W. Hutchinson, Acta Metallurgica Et Materialia **42,** 475-487 (1994).

[32] N. Tamura, A. A. MacDowell, R. Spolenak, B. C. Valek, J. C. Bravman, W. L. Brown, R. S. Celestre, H. A. Padmore, B. W. Batterman, and J. R. Patel, Journal of Synchrotron Radiation **10,** 137-143 (2003).

[33] A. S. Budiman, W. D. Nix, N. Tamura, B. C. Valek, K. Gadre, J. Maiz, R. Spolenak, and J. R. Patel, Applied Physics Letters **88,** 233515 (2006).

[34] B. C. Valek, Ph.D. Thesis, Stanford University, 2003.

[35] W. Yang, B. C. Larson, G. M. Pharr, G. E. Ice, J. D. Budai, J. Z. Tischler, and W. J. Liu, Journal of Materials Research **19,** 66-72 (2004).

[36] W. Yang, B. C. Larson, G. M. Pharr, G. E. Ice, J. G. Swadener, J. D. Budai, J. Z. Tischler, and W. Liu, Materials Research Society Symposium - Proceedings **750,** 115-118 (2002).

[37] W. Yang, B. C. Larson, G. M. Pharr, G. E. Ice, J. Z. Tischler, J. D. Budai, and W. Liu, Materials Research Society Symposium - Proceedings **779,** 207-212 (2003).

[38] W. Yang, B. C. Larson, J. Z. Tischler, G. E. Ice, J. D. Budai, and W. Liu, Micron **35,** 431-439 (2004).

[39] R. Barabash, G. E. Ice, B. C. Larson, G. M. Pharr, K. S. Chung, and W. Yang, Applied Physics Letters **79,** 749-751 (2001).

[40] R. I. Barabash, G. E. Ice, B. C. Larson, and W. G. Yang, Review of Scientific Instruments **73,** 1652-1654 (2002).

[41] I. Horcas, R. Fernandez, J. M. Gomez-Rodriguez, J. Colchero, J. Gomez-Herrero, and A. M. Baro, Review of Scientific Instruments **78,** 013705 (2007).

[42] A. S. Budiman, S. M. Han, J. R. Greer, N. Tamura, J. R. Patel, and W. D. Nix, Acta Materialia **submitted** (2007).

[43] Y. Huang, F. Zhang, K. C. Hwang, W. D. Nix, G. M. Pharr, and G. Feng, Journal of the Mechanics and Physics of Solids **54,** 1668-1686 (2006).

[44] A. Bolshakov and G. M. Pharr, Journal of Materials Research **13,** 1049-1058 (1998).

[45] Y. T. Cheng and C. M. Cheng, Materials Science & Engineering R-Reports **44,** 91-149 (2004).

[46] G. Feng and W. D. Nix, Scripta Materialia **51,** 599-603 (2004).

[47] Y. Liu and A. H. W. Ngan, Scripta Materialia **44,** 237-241 (2001).

[48] K. L. Johnson, *Contact mechanics* (Cambridge University Press, 1987).

[49] G. Feng, S. Qu, Y. Huang, and W. D. Nix, Acta Materialia **55,** 2929-2938 (2007).

[50] Y. Y. Lim and M. M. Chaudhri, Philosophical Magazine a-Physics of Condensed Matter Structure Defects and Mechanical Properties **79,** 2979-3000 (1999).